The Astrophysical Journal, 909:2 (7pp), 2021 March 1 https://doi.org/10.3847/1538-4357/abda51

LOFAR Observations of a Jet-driven Piston Shock in the Low Solar Corona

Ciara A. Maguire[1,2], Eoin P. Carley[2], Pietro Zucca[3], Nicole Vilmer[4,5], and Peter T. Gallagher[2]
[1] School of Physics, Trinity College Dublin, Dublin 2, Ireland
[2] Astronomy & Astrophysics Section, Dublin Institute for Advanced Studies, Dublin, D02 XF86, Ireland
[3] ASTRON Netherlands Institute for Radio Astronomy, Dwingeloo, The Netherlands
[4] LESIA, Observatoire de Paris, PSL Research University, CNRS, Sorbonne Universitès, UPMC Univ. Paris 06, Univ. Paris Diderot, Sorbonne Paris Citè, 5 place Jules Janssen, F-92195 Meudon, France
[5] Station de Radioastronomie de Nançay, Observatoire de Paris, PSL Research University, CNRS, Univ. Orlèans, F-18330 Nançay, France
Received 2020 October 12; revised 2021 January 2; accepted 2021 January 6; published 2021 March 1

Abstract

The Sun produces highly dynamic and eruptive events that can drive shocks through the corona. These shocks can accelerate electrons, which result in plasma emission in the form of a type II radio burst. Despite the large number of type II radio burst observations, the precise origin of coronal shocks is still subject to investigation. Here, we present a well-observed solar eruptive event that occurred on 2015 October 16, focusing on a jet observed in the extreme ultraviolet by the Atmospheric Imaging Assembly (SDO/AIA), a streamer observed in white light by the Large Angle and Spectrometric Coronagraph (SOHO/LASCO), and a metric type II radio burst observed by the LOw Frequency Array (LOFAR). LOFAR interferometrically imaged the fundamental and harmonic sources of a type II radio burst and revealed that the sources did not appear to be cospatial, as would be expected from the plasma emission mechanism. We correct for the separation between the fundamental and harmonic using a model that accounts for scattering of radio waves by electron density fluctuations in a turbulent plasma. This allows us to show the type II radio sources were located $\sim 0.5 R_{\odot}$ above the jet and propagated at a speed of $\sim 1000\ \mathrm{km\ s^{-1}}$, which was significantly faster than the jet speed of $\sim 200\ \mathrm{km\ s^{-1}}$. This suggests that the type II burst was generated by a piston shock driven by the jet in the low corona.

Unified Astronomy Thesaurus concepts: Active solar corona (1988); Solar radio emission (1522); Shocks (2086); Radio bursts (1339); Plasma jets (1263); Solar flares (1496); Solar coronal streamers (1486); Solar extreme ultraviolet emission (1493)

Supporting material: animation

1. Introduction

The Sun regularly produces a variety of highly dynamic and energetic explosive events such as coronal mass ejections (CMEs), flares, erupting loops or plasmoids, ejecta-like sprays, and jets (Klein et al. 1999; Dauphin et al. 2006; Zimovets et al. 2012; Carley et al. 2013; Morosan et al. 2019; Chrysaphi et al. 2020; Maguire et al. 2020). The mass motions during these eruptive events can often travel with speeds that exceed the local background Alfvèn speed, which results in the formation of plasma shocks. The acceleration of electrons at the shock front can prompt coherent plasma emission at both the fundamental (f_p) and second harmonic ($2f_p$) of the plasma frequency (Nelson & Melrose 1985; Vršnak & Cliver 2008). The radio emission produced in this process is referred to as a type II radio burst, and since the plasma frequency f_p is dependent upon the background electron density n_e via $f_p \approx 9000\sqrt{n_e(\mathrm{cm^{-3}})}$ MHz, type II bursts provide a useful diagnostic of local coronal conditions and shock parameters. Furthermore, observations of type II bursts can provide insight into the origin of coronal shocks and help us determine whether they are (1) flare related due to blast waves, or (2) CME or small-scale ejecta related (Zimovets et al. 2012; Eselevich et al. 2015; Mancuso et al. 2019). The shock can be further classified as a bow shock or a piston-driven shock. For the bow shock scenario, the ambient plasma is able to flow around the driver so that the shock and driver are seen to propagate at the same velocity (Cho et al. 2007; Schmidt et al. 2016). In the case of a piston-driven shock, the plasma is unable to flow behind the driver so that the distance between the driver and shock increases with time and the shock speed can be several times that of the driver (Pomoell et al. 2008; Nindos et al. 2011; Bain et al. 2012; Grechnev et al. 2018).

To date, the origin of plasma shocks has predominantly been studied in terms of highly energetic events, namely strong flares (Zucca et al. 2018), X-ray jets (Klein et al. 1999), erupting coronal loops (Dauphin et al. 2006), eruptive magnetic flux rope (Wang et al. 2019), plasmoids (Bain et al. 2012; Carley et al. 2013), and CMEs (Maguire et al. 2020). However, few studies have investigated type II bursts associated with EUV jets and weak CMEs (see Chrysaphi et al. 2020 as an example). Here, we present observations of a C-class flare and a narrow jet that resulted in a metric type II radio burst. We determine the location of the type II burst and carry out a multiwavelength kinematic analysis to infer the origin of the shock.

Our kinematic analysis includes an investigation of low-frequency radio wave scattering in the corona, which is necessary to account for radio source displacements from their true position. Early observations by the Culgoora Radioheliograph revealed that type II fundamental emission is radially shifted outwards with respect to harmonic emission (Kai & McLean 1968; Sheridan et al. 1972; Nelson & Sheridan 1974; Nelson & Robinson 1975; Suzuki et al. 1985). Such behavior is attributed to radio wave scattering (Fokker 1963; Steinberg et al. 1971; Stewart 1972; Riddle 1974; Bastian 1994). More recently, LOw Frequency Array (LOFAR; van Haarlem et al. 2013) tied-array beam observations demonstrated that band-split type II fundamental sources experience displacement due to radio wave scattering in a turbulent medium (Chrysaphi et al. 2018). In this study, we use LOFAR interferometric observations, which have superior spatial

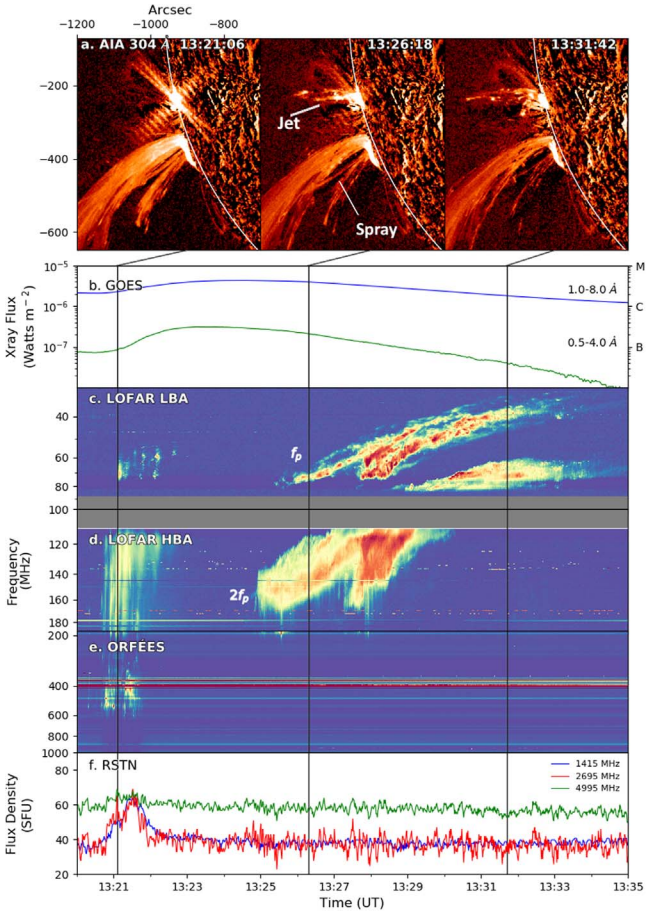

Figure 1. (a) Base difference images of the jet and spray observed with AIA 304 Å. (b) GOES 0.5–4 Å and 1–8 Å soft X-ray flux of the C4.3 class solar flare. The remaining panels show the radio emission as observed by (c) LOFAR's low-band antennae (LBA; 30–90 MHz), (d) LOFAR's high band antennae (HBA; 110–240 MHz), (e) ORFÈES (140–1000 MHz), and (f) RSTN channels (1415 MHz, 2695 MHz, and 4995 MHz). The LOFAR dynamic spectra show a type II radio burst with fundamental (f_p) and harmonic ($2f_p$) components initiating at 13:25 UT and ceasing at 13:34 UT.

resolution with respect to tied-array observations, to image the separation between type II fundamental and harmonic components with unprecedented spatial and temporal resolution. We account for the spatial displacement between fundamental and harmonic sources using a model of radio wave scattering in the corona that allows for a necessary correction of radio source positions and their comparison with the shock driver imaged in the EUV, showing they follow the kinematics of a piston-driven shock.

In Section 2, observations of the flare, jet, and type II radio burst are presented. The observational method and models used to determine the radio source location are described in Section 3. We discuss the shock origin and the nature of radio wave scattering in Section 4, and finally, conclusions are presented in Section 5.

2. Observations

A GOES C4.3 class flare (Figure 1(b)) began 2015 October 16 at 13:20 UT from active region NOAA 12435 (SOL2015-10-16T13:25:30). The flare was located on the solar eastern limb, and inspection of data from the Extreme Ultraviolet Imager (EUVI; Wuelser et al. 2004) on board the STEREO-A spacecraft near the time of the flare revealed that the active region extended around the far side of the Sun. Base difference images shown in Figure 1(a) from the 304 Å passband of the Atmospheric Imaging Assembly (AIA; Lemen 2012) on board the Solar Dynamics Observatory (SDO; Pesnell et al. 2012) illustrate the evolution of a jet that emerged from the active region during the impulsive phase of the flare. The jet originates from a foot point on the limb, meaning it most likely propagated close to the plane of sky (POS). The ejected material initially moved radially before moving slightly southward. Below the jet, a spray-like feature was observed to propagate in a southward direction. The spray emerged an hour prior to the flare and persisted for the duration of the eruption.

In Figures 1(c)–(f) the spectral radio observations from various ground instruments are shown, namely LOFAR's remote station RS509 observing between 10 MHz and 240 MHz, the radio spectrograph Observation Radio Frequence pour l'Ètude des Eruptions Solaires (ORFÈES),[6] observing between 140 MHz and 1000 MHz, and the Learmonth site of the Radio Solar Telescope Network (RSTN)[7] measuring solar radio flux density. Coinciding with the onset of the GOES X-ray at 13:20 UT, a group of type IIIs was detected by LOFAR and ORFÈES, as shown in panels (c)–(e). Subsequently at ∼13:25 UT, LOFAR observed a strong type II radio burst with well-defined fundamental and first harmonic emission bands, indicated in Figures 1(c) and (d) by f_p and $2f_p$, respectively. Both the fundamental and harmonic emission bands exhibit detailed structure, band splitting, and fragmentation into multiple bands with different drift rates. At the time of the type II burst there was no significant radio emission above 200 MHz (see panels e and f), which suggests that no radio emission was generated or escaped from low in the corona and that the flare may have been partially occulted. Unfortunately there were no STEREO-A images at the time of the eruption to observe the evolving active region.

LOFAR also provided interferometric observations of the event until 14:00 UT using the low-band antennas (10–90 MHz) from 36 stations (24 core and 16 remote). The maximum baseline of the LOFAR observation was 84 km, which gave subarcminute resolution across almost all of the observed frequency range. Observations of the calibrator source, Virgo A, were taken simultaneously over all subbands. The visibility data was recorded with a correlator integration time of 0.167 s (Zhang et al. 2020). The data was processed using the Default Processing Pipeline (van Diepen et al. 2018), followed by an implementation of WSCLEAN[8] (Offringa et al. 2014) to produce images with a spectral resolution of 195.3 kHz and cadence of 1 s.

3. Data Analysis and Results

In the following, we determine the location of the fundamental and harmonic components of the type II burst in relation to the jet observed in the EUV. This can only be done after accounting for radio wave propagation effects, allowing us to determine where the radio burst was generated in relation to the eruptive structure and the kind of coronal environment that lead to shock formation.

[6] http://secchirh.obspm.fr/spip.php?article19
[7] http://www.ngdc.noaa.gov
[8] https://gitlab.com/aroffringa/wsclean/

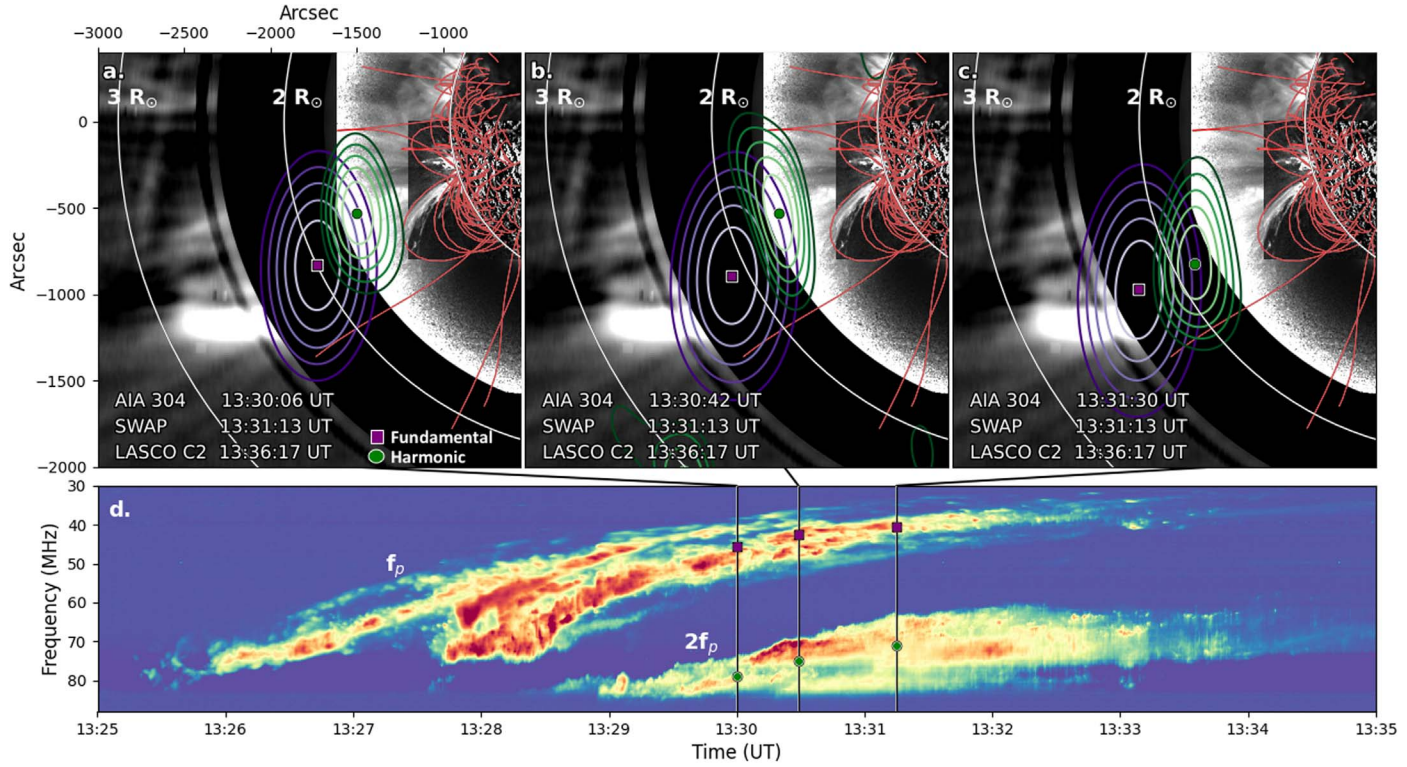

Figure 2. (a)–(c) Type II radio burst observed by LOFAR at three separate times. The purple and green contours represent 50–90% the peak flux density of the fundamental (f_p) and harmonic ($2f_p$) radio sources, respectively. The purple square and green dot represent the bursts' centroid position. The burst contours are overlaid on composite images from AIA 304 Å images (innermost), SWAP 174 Å (central), and LASCO C2 (outermost). The coronal magnetic field determined from the PFSS is shown by red lines. The solid white circles indicate distances of $2R_\odot$ and $3R_\odot$. (d) The corresponding dynamic spectrum showing the f_p and $2f_p$ components. Purple squares and green dots denote the points along the burst that have been imaged.

3.1. Imaging of Radio Burst

In order to track the motion of the shock, we image the fundamental and harmonic components of the type II burst at multiple moments in time. Figure 2(a)–(c) illustrates the position of the fundamental (purple contours) and harmonic (green contours) component of the type II burst overlaid on composite images from AIA 304 Å (innermost), Sun Watcher using Active Pixel (SWAP; Berghmans et al. 2006) 174 Å (central), and LASCO C2 (outermost). The red lines represent the Sun's coronal magnetic field, which was extrapolated from the photospheric magnetic field using the Potential-Field Source-Surface model (PFSS; Stansby et al. 2020) with data from the Global Oscillation Network Group (GONG; Harvey et al. 1996). Figure 2(d) demonstrates the type II radio burst dynamic spectrum with the fundamental and harmonic emission bands labeled as f_p and $2f_p$, respectively. The purple squares and green dots indicate the points imaged along the burst as seen in panels a–c. The imaging reveals that the fundamental source (purple contours) is shifted radially outwards with respect to the harmonic source (green contours) by 0.3–0.5 $R_\odot$. We find that regardless of where we image on the emission bands at one particular time, there is a clear separation between the fundamental and harmonic sources. Such behavior contradicts the underlying plasma emission mechanism according to which fundamental and harmonic radio waves are generated in the same location and should therefore appear cospatial (Melrose 1975). The observed displacement is potentially due to the scattering of radio waves by electron density fluctuations that exist due to turbulent plasma processes in the corona (Steinberg et al. 1971; Stewart 1972; Nelson & Sheridan 1974; Riddle 1974). Scattering effects are particularly significant on fundamental (as opposed to harmonic) radio waves because the fundamental emission is close to the plasma frequency and therefore is strongly affected by propagation effects, e.g., due to small-scale variations in the background density of the plasma. This variation in the background density determines the level of scattering of radio waves and is described by the relative level of root mean squared (rms) density fluctuations $\varepsilon = \sqrt{\langle \delta n^2 \rangle}/n$, where n is the electron density.

In the next section we account for the effects of scattering on fundamental emission to correctly interpret the type II observations for this event and in the process gain insight into the parameters that describe radio wave scattering.

3.2. Scattering of Fundamental Plasma Emission

The dynamic spectrum presented in Figure 3(a) shows the type II fundamental and harmonic emission bands marked with purple squares and green circles, respectively, with dark-to-light shading representing progression in time. The time-frequency points were selected using a fundamental to harmonic frequency ratio of 1.8–1.9, to be consistent with observations (Melnik et al. 2018). Panels (b) and (c) depict the positions of the fundamental and harmonic sources on a composite image from AIA 304 Å, SWAP 174 Å, and LASCO C2. The coronal magnetic field determined from the PFSS is shown by red lines. Here, we assume the displacement between the fundamental and harmonic emission is caused by radio wave scattering. To estimate the extent to which the fundamental is shifted by scattering, we adopt the Chrysaphi et al. (2018) model. This model assumes that as radio waves propagate through the corona they undergo repeated small-angle deflections due to isotropic fluctuations in the plasma density

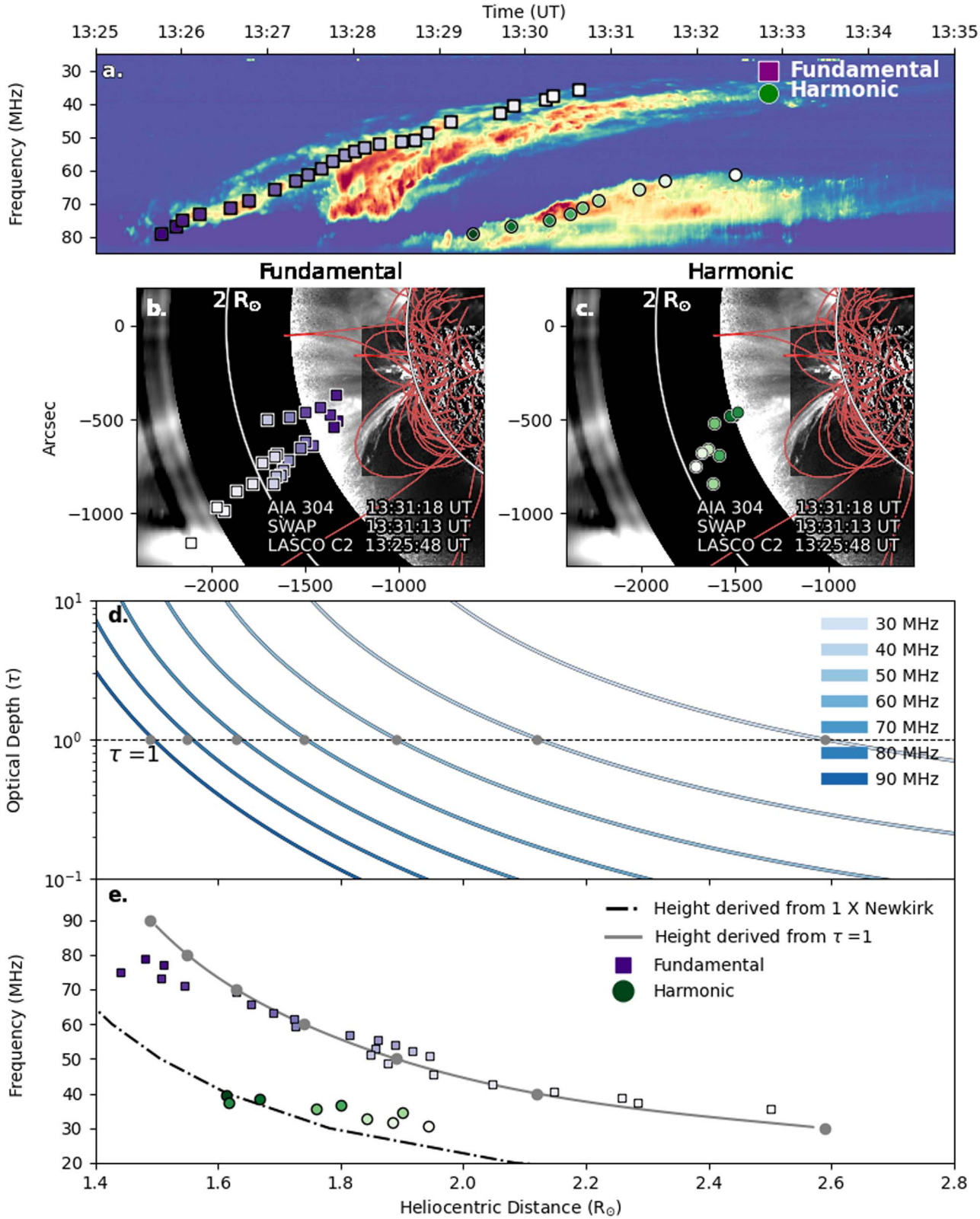

Figure 3. (a) LOFAR dynamic spectrum depicting the fundamental (f_p) and harmonic emission ($2f_p$) of a type II burst. The purple squares and green circles overlaid illustrate the frequency and times of the burst that were imaged, with dark-to-light shading representing progression in time. (b) and (c) The centroids of the fundamental (purple squares in (b)) and harmonic component (green circles in (c)) of the type II burst overlaid on an EUV and WL composite image from SDO/AIA 304 Å, PROBA2/SWAP 174 Å, and SOHO/LASCO C2. The coronal magnetic field determined from the PFSS is shown by red lines. (d) The optical depth with respect to scattering for radio waves as a function of heliocentric distance for a range frequencies between 30 MHz and 90 MHz. The dashed line indicates $\tau = 1$ and the gray dots indicate the height at which the radio source is predicted to appear for each frequency. (e) The heights of fundamental (purple squares) and harmonic (green dots) sources as observed by LOFAR. The gray line represents where the scattering model predicts the fundamental radiation eventually escapes and the dashed black line represents where the emission is generated, as predicted by the Newkirk model.

caused by turbulence (see Gordovskyy et al. 2019 for details). The optical depth with respect to scattering for radio waves in the corona is described as

$$\tau(r) = \int_{r}^{1AU} \pi \frac{f_p^4(r)}{(f^2 - f_p^2(r))} \frac{\varepsilon^2}{h} dr \quad (1)$$

where f_p is the plasma frequency, h is the effective scale length of density fluctuations, and ε is relative level of electron density fluctuations.[9] A given model of f_p predicts where the emission is generated, and where we expect to see harmonic emission, since it undergoes very little scattering. The Newkirk model best describes the positions of the harmonic sources, assuming the shock propagated close to POS (see Figure 3(e)). Considering Equation (1), $\tau(r) = 1$ corresponds to the heliocentric distance at which fundamental radio emission is expected to escape. The value of ε^2/h was obtained from optimizing the fit between the heights predicted at $\tau = 1$ with the radial positions of the fundamental emission. Using this approach, ε^2/h was found to be $2 \times 10^5\ \mathrm{km}^{-1}$.

Figure 3(d) illustrates the solution to Equation (1), showing how τ varies with r for different values of f (f in the range 30–90 MHz in steps of 10 MHz). The dashed line indicates the point at which $\tau(r) = 1$. The expected height of scattered fundamental emission at each frequency is marked by a gray dot. In Figure 3(e), the gray line represents where the model predicts the fundamental radiation eventually escapes. The dashed black line is where the emission is generated (according to the Newkirk model), and where the harmonic emission should be observed. The heights of fundamental sources (purple squares) agree quite well with the scattering model (gray line) while the harmonic sources (green dots) are in agreement with the Newkirk model (dashed black line). This shows the spatial displacement of these radio sources is accounted for by the scattering model.

It should be noted that there is a deviation between the models and data at higher frequencies and this may be an effect of the Newkirk model's inability to accurately describe the complex structure of the low corona. There are a plethora of density models such as Mann, Baumbach–Allen, and Saito, however these models predict even lower densities at these heights (Baumbach 1937; Allen 1947; Saito et al. 1970; Mann et al. 1999). The Newkirk model was therefore established as the most appropriate to describe the observed source positions.

To summarize, LOFAR provided images of the fundamental and harmonic emission so that we are able to identify where the radio waves were generated (location of harmonic) as well as where the scattered radio waves escaped (location of fundamental). Overall the Chrysaphi et al. (2018) model successfully accounts for the spatial separation between the fundamental and harmonic emission. The model proves to be a reliable means to correct for the positional shift due to scattering, so that we can accurately determine the type II burst kinematics.

[9] Equation (1) is adopted from Equation (9) of Chrysaphi et al. (2018), where we have assumed a power-law spectrum of electron density fluctuations, which is more consistent with in situ observations (Bastian 1994). This means that the coefficient $\sqrt{(\pi)}/2$ is now π, following Equation (31) of Thejappa et al. (2007) and Equation (34) of Thejappa & MacDowall (2008).

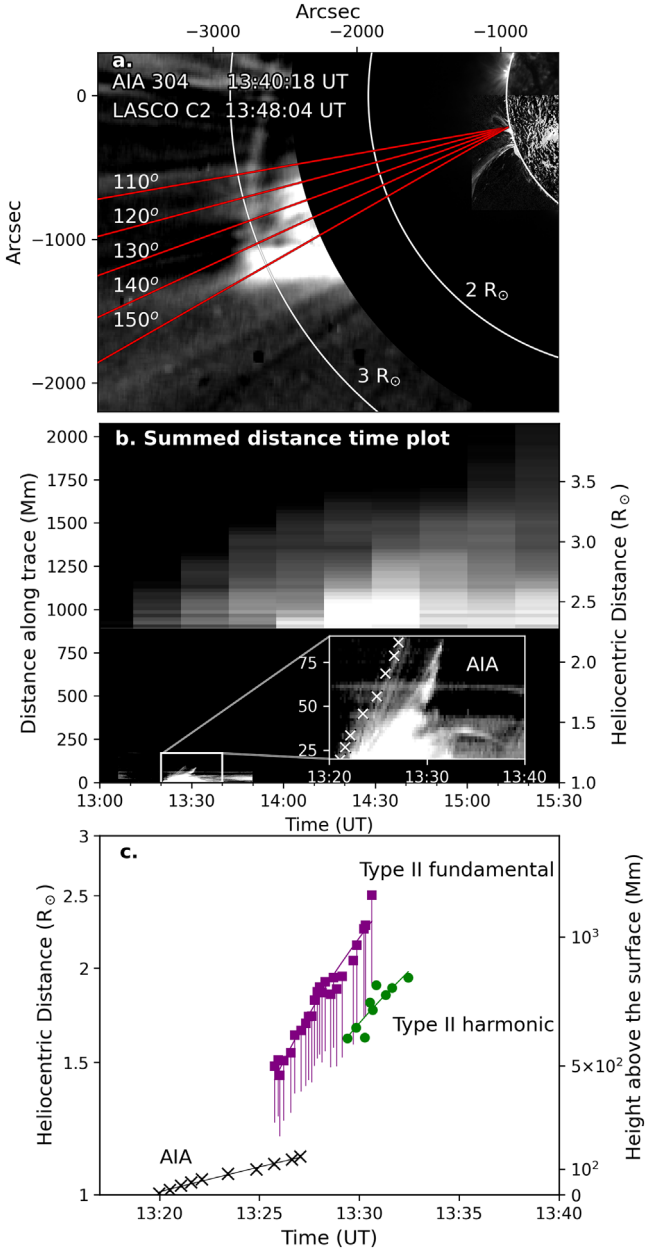

Figure 4. (a) Composite of base difference images from AIA 304 Å and LASCO C2, with five red traces over the region of interest. The traces start 110° to the solar north and are separated by 10°. (b) The sum of the time–distance plots generated along the five traces and a zoom-in of the AIA field of view. (c) The height–time profiles of the EUV and radio features. The jet as seen by AIA is marked by black crosses and the position of the fundamental and harmonic type II radio emission are marked by purple squares and green dots, respectively. The error bars associated with the fundamental emission represent the scattering induced radial displacement. An animation of the LASCO C2 images is available in the online Journal. The animation runs from 12:12 to 17:48 UT.

(An animation of this figure is available.)

3.3. Kinematics of Ejecta and Type II Radio Burst

Figure 4(a) presents a composite of base difference images from SDO/AIA 304 Å and LASCO C2 showing the jet on the solar limb and an overarching helmet streamer situated ~100° to solar north. To determine the ejecta kinematics, five traces were examined around the region of interest, indicated by five red lines in Figure 4(a). The traces originate at the active region from the

solar limb, starting 110° to the solar north, and are separated by 10°. The distance–time plot associated with each of the traces was summed to produce the plot illustrated in Figure 4(b). The inset is a zoom-in on the AIA field of view showing the jet, which appears to have a few components, as indicated by the two-prong structure. We take the foremost component as a measure of the jet front. The crosses overlaid on Figure 4(b) indicate the points selected using a point-and-click technique. The fundamental and harmonic emission heights were taken as the distance between the source centroid and solar center. Combing the EUV and radio data, a height–time profile was constructed as shown in Figure 4(c). The jet is marked by black crosses and the height of the type II fundamental and harmonic emission are marked by purple squares and green dots, respectively. The error bar associated with the fundamental emission represents the scattering induced radial shift, as calculated in Section 3.2. The error associated with the EUV heights was deduced from 10 trial measurements of height in Figure 4(b) and was found to be $\sim 0.1 R_\odot$ ($\sim$10 pixels). The jet was observed to have an average velocity of $\sim 200\,\mathrm{km\,s^{-1}}$ and the type II fundamental and harmonic traveled at $\sim 1000\,\mathrm{km\,s^{-1}}$ and $\sim 1090\,\mathrm{km\,s^{-1}}$, respectively. The significance of these results are discussed in Section 4.1. We note that although there is slight movement in the streamer observed by LASCO C2 (see the online animation associated with Figure 4), it is unclear whether this is associated with the motion that lead to the type II burst; therefore, we concentrate on the kinematics of the jet and type II burst in this study.

4. Discussion

4.1. What is the Origin of the Shock?

As seen in Figure 1, the EUV jet emerged at 13:20 UT from the solar limb and propagated outwards at a speed of $\sim 200\,\mathrm{km\,s^{-1}}$. Although the jet initially moved radially, the PFSS in Figures 3(b) and (c) suggests that the ejected material later moved southward due to the closed magnetic field lines. About five minutes later, the type II burst was observed $\sim 0.5 R_\odot$ above the jet and had a significantly larger velocity ($\sim 1000\,\mathrm{km\,s^{-1}}$), which is indicative of a piston-driven shock (Liepmann & Roshko 1957; Maxwell et al. 1985; Pomoell et al. 2008; Vršnak & Cliver 2008). We note that we have based this analysis on the assumption that the driver and shock propagate close to the POS; even if this was not precisely the case, our interpretation is still valid. For example, if the shock propagated at an angle of 20° from the plane of sky, the shock speed would still exceed the speed of the driver, which is characteristic of a piston-driven shock.

We found the local Alfvèn speed in the region of interest by combining the Newkirk electron density model and a 2D plane-of-sky magnetic field map (derived from a PFSS model). Considering the same five traces in Figure 4(a), the average Alfvèn speed at $2R_\odot$ was found to be $740 \pm 70\,\mathrm{km\,s^{-1}}$. The fact the jet (shock driver) propagated at sub-Alfvènic velocities ($\sim 200\,\mathrm{km\,s^{-1}}$) provides further evidence that the shock was piston driven (Vršnak & Cliver 2008). The Alfvèn Mach number M_A of the shock was estimated to be $\sim$1.35 by taking the ratio of the shock speed ($\sim 1000\,\mathrm{km\,s^{-1}}$) to Alfvèn speed ($740 \pm 70\,\mathrm{km\,s^{-1}}$). This M_A value is consistent with previous studies (Vršnak et al. 2001; Zucca et al. 2014; Maguire et al. 2020). The M_A was also estimated from the band splitting seen in the type II fundamental emission band at 13:27:30–13:30:00 UT. Using the relative instantaneous bandwidth between the upper and lower split bands, the compression ratio X was found to be in the range 1.3–1.5. To determine M_A values, we used the expression from Vršnak et al. (2002) for a perpendicular shock:

$$M_\mathrm{A} = \sqrt{\frac{X(X + 5 + 5\beta)}{2(4 - X)}} \tag{2}$$

where β is the plasma-to-magnetic pressure ratio ($\beta \ll 1$). The values for M_A were found to be 1.3–1.4, which is consistent with M_A derived from the shock speed to Alfvèn speed ratio.

In summary, we suggest that as the jet erupted, a piston-driven shock was established ahead of it and the streamer may have acted as a tube for the shock to propagate down (Eselevich et al. 2015). Piston-driven shocks with type II emission have often been associated with wide and fast CME drivers (Kahler et al. 2019), but few have reported piston shocks resulting from narrow ejecta low in the corona as is the case in this event.

4.2. Radio Wave Scattering in the Low Corona

In Section 3.2 we showed that the scattering model successfully accounts for the spatial separation between the type II fundamental and harmonic emission. Let us consider the validity of the model's assumptions, namely, that scattering is the dominant radio wave propagation effect in the low corona and that scattering is due to isotropic density fluctuations.

We provide evidence that scattering is the dominant propagation effect on radio waves by comparing the size of the fundamental and harmonic sources, normalized to the point-spread function of LOFAR (see Figures 2(a)–(c)). The fundamental sources were found to be 1.6–1.9 times larger than the harmonic sources. This is as expected, since scattering from density fluctuations is known to have a more significant effect on the fundamental emission rather than on the harmonic (Nelson & Robinson 1975; Lengyel-Frey et al. 1985).

The model used in this work also assumes radio wave scattering by isotropic density fluctuations. However, previous work suggests that density fluctuations are in fact anisotropic, which would imply ε^2/h has both a parallel and a perpendicular component (Armstrong et al. 1990; Anantharamaiah et al. 1994). In order to determine whether this assumption changes our results, we consider the effects of anisotropic scattering on radio sources. Numerical models by Kontar et al. (2019) suggest the radial shift experienced by a radio source due to anisotropic scattering is slightly less than in the isotropic scenario ($\sim 0.52 R_\odot$ compared to $\sim 0.68 R_\odot$ for a source propagating in POS). To account for the displacement under anisotropic scattering conditions, the values of ε^2/h would have to be slightly larger. It is important to note that although anisotropy does not have a dramatic effect on the radial shift, it does affect source morphology, e.g., sources are expected to elongate perpendicular to the heliospheric radial direction due to enhanced scattering perpendicular to the large-scale (radial) magnetic field of the Sun or elongated sources (Ingale et al. 2015; Kontar et al. 2017).

While the simple analytical model used in this analysis can successfully account for shifted positions of the radio sources, it cannot account for all observed properties of scattered sources (for example, size and morphology). As such, future studies that combine fully developed numerical scattering models with interferometric observations from LOFAR are needed to comprehensively understand radio wave propagation in the turbulent plasma near coronal shocks.

5. Conclusion

We present a study of a flare, jet, and type II radio burst that occurred on 2015 October 16 on the eastern limb of the Sun. The purpose of this study was to determine the location of the type II burst and the origin of the associated plasma shock. We carried out a multiwavelength kinematic analysis, which included an investigation of low-frequency radio wave scattering in the corona. LOFAR interferometrically imaged both the fundamental and harmonic emission of a metric type II and revealed that the sources are not cospatial, as would be expected from the plasma emission mechanism. We account for their spatial displacement using a model of radio scattering in the corona. This model allowed for necessary correction of source positions and their comparison with the shock driver. Furthermore, optimization of the model to the data provided information about scattering parameters in particular the level of density fluctuations in the turbulent corona, e.g., we found that $\varepsilon^2/h \sim 2 \times 10^5\,\mathrm{km}^{-1}$, which is slightly lower compared to that found in previous studies (Chrysaphi et al. 2018).

After accounting for radio wave scattering effects, we determined where the radio burst was generated in relation to the eruptive structure and the coronal environment that lead to shock formation. We found that the type II burst was located at a much higher altitude than the EUV jet and had a significantly larger velocity, namely the jet speed was $\sim$200 km s^{-1} while the type II burst propagated at $\sim$1000 km s^{-1}. The association of the sub-Alfvènic jet with the type II burst and the relative velocities of the jet and the type II emission provides strong evidence of a shock that was initially piston driven.

C.A.M. is supported by an Irish Research Council Government of Ireland Postgraduate Scholarship. We are grateful to the GOES, AIA, SWAP, and LASCO teams for open access to their data. The data sets generated during and/or analyzed during the current study are available in the LOFAR Long Term Archive, https://lta.lofar.eu/ and https://sdo.gsfc.nasa.gov/data/. ORFÈES is part of the FEDOME project, partly funded by the French Ministry of Defense. We would like to thank Ambassade de France in Ireland for providing a high-level scientific mobility grant to allow for part of this work to be carried out in LESIA, Observatoire de Paris, France. The Irish LOFAR Consortium and Ireland's membership of the International LOFAR Telescope are supported by Science Foundation Ireland and the Department of Further and Higher Education, Research, Innovation and Science.

ORCID iDs

Ciara A. Maguire https://orcid.org/0000-0001-9564-6151
Eoin P. Carley https://orcid.org/0000-0002-6106-5292
Pietro Zucca https://orcid.org/0000-0002-6760-797X
Nicole Vilmer https://orcid.org/0000-0002-6872-3630
Peter T. Gallagher https://orcid.org/0000-0001-9745-0400

References

Allen, C. W. 1947, MNRAS, 107, 426
Anantharamaiah, K. R., Gothoskar, P., & Cornwell, T. J. 1994, JApA, 15, 387
Armstrong, J. W., Coles, W. A., Rickett, B. J., & Kojima, M. 1990, ApJ, 358, 685
Bain, H. M., Krucker, S., Glesener, L., & Lin, R. P. 2012, ApJ, 750, 44
Bastian, T. S. 1994, ApJ, 426, 774
Baumbach, S. 1937, AN, 263, 121
Berghmans, D., Hochedez, J. F., Defise, J. M., et al. 2006, AdSpR, 38, 1807
Carley, E. P., Long, D. M., Byrne, J. P., et al. 2013, NatPh, 9, 811
Cho, K.-S., Gary, D. E., Lee, J., Moon, Y.-J., & Park, Y. D. 2007, ApJ, 665, 799
Chrysaphi, N., Kontar, E. P., Holman, G. D., & Temmer, M. 2018, ApJ, 868, 10
Chrysaphi, N., Reid, H. A. S., & Kontar, E. P. 2020, ApJ, 893, 115
Dauphin, C., Vilmer, N., & Krucker, S. 2006, A&A, 455, 339
Eselevich, V. G., Eselevich, M. V., Sadykov, V. M., & Zimovets, I. V. 2015, AdSpR, 56, 2793
Fokker, A. D. A. 1963, SSRv, 2, 70
Gordovskyy, M., Kontar, E., Browning, P., & Kuznetsov, A. 2019, ApJ, 873, 48
Grechnev, V. V., Lesovoi, S. V., Kochanov, A. A., et al. 2018, JASTP, 174, 46
Harvey, J. W., Hill, F., Hubbard, R. P., et al. 1996, Sci, 272, 1284
Ingale, M., Subramanian, P., & Cairns, I. 2015, MNRAS, 447, 3486
Kahler, S. W., Ling, A. G., & Gopalswamy, N. 2019, SoPh, 294, 1
Kai, K., & McLean, D. J. 1968, PASA, 1, 141
Klein, K. L., Khan, J. I., & Vilmer, N. 1999, A&A, 346, L53
Kontar, E. P., Chen, X., Chrysaphi, N., et al. 2019, ApJ, 884, 122
Kontar, E. P., Yu, S., Kuznetsov, A. A., et al. 2017, NatCo, 8, 1
Lemen, J. R. 2012, SoPh, 275, 17
Lengyel-Frey, D., Stone, R. G., & Bougeret, J. L. 1985, A&A, 151, 215
Liepmann, H., & Roshko, A. 1957, Elements of Gasdynamics (New York: Wiley)
Maguire, C. A., Carley, E. P., McCauley, J., & Gallagher, P. T. 2020, A&A, 633, A56
Mancuso, S., Frassati, F., Bemporad, A., & Barghini, D. 2019, A&A, 624, 2
Mann, G., Jansen, F., Macdowall, R. J., Kaiser, M. L., & Stone, R. G. 1999, A&A, 348, 614
Maxwell, A., Dryer, M., & McIntosh, P. 1985, SoPh, 97, 401
Melnik, V. N., Brazhenko, A. I., Frantsuzenko, A. V., Dorovskyy, V. V., & Rucker, H. O. 2018, SoPh, 293, 26
Melrose, D. B. 1975, SoPh, 43, 79
Morosan, D. E., Carley, E. P., Hayes, L. A., et al. 2019, NatAs, 3, 452
Nelson, G., & Robinson, R. D. 1975, PASA, 2, 370
Nelson, G. J., & Melrose, D. B. 1985, in Solar Radiophysics: Studies of Emission from the Sun at Metre Wavelengths, ed. D. J. McLean & N. R. Labrum (Cambridge: Cambridge Univ. Press), 333
Nelson, G. J., & Sheridan, K. V. 1974, Coronal Disturbances (Dordrecht: Springer), 345
Nindos, A., Alissandrakis, C. E., Hillaris, A., & Preka-Papadema, P. 2011, A&A, 531, 531
Offringa, A. R., Kinley, B., Hurley-Walker, N., et al. 2014, MNRAS, 444, 606
Pesnell, W. D., Thompson, B. J., & Chamberlin, P. C. 2012, SoPh, 275, 3
Pomoell, J., Vainio, R., & Kissmann, R. 2008, SoPh, 253, 249
Riddle, A. C. 1974, SoPh, 35, 153
Saito, K., Makita, M., Nishi, K., & Hata, S. 1970, AnTok, 12, 51
Schmidt, J. M., Cairns, I. H., Gopalswamy, N., & Yashiro, S. 2016, JGRA, 121, 9299
Sheridan, K. V., Labrum, N. R., & Payten, W. J. 1972, NPhS, 238, 115
Stansby, D., Yeates, A., & Badman, S. 2020, JOSS, 5, 2732
Steinberg, J. L., Aubier-Giraud, M., Leblanc, Y., & Boischot, A. 1971, A&A, 10, 362
Stewart, R. T. 1972, PASA, 2, 100
Suzuki, S., & Dulk, G. A. 1985, Solar Radiophysics (Cambridge: Cambridge Univ. Press), 289
Thejappa, G., & MacDowall, R. J. 2008, ApJ, 676, 1338
Thejappa, G., MacDowall, R. J., & Kaiser, M. L. 2007, ApJ, 671, 894
van Diepen, G., Dijkema, T. J., & Offringa, A. 2018, Astrophysics Source Code Library DPPP: Default Pre-Processing Pipeline, ascl:1804.003
van Haarlem, M. P., Wise, M. W., Gunst, A. W., et al. 2013, A&A, 556, A2
Vršnak, B., Aurass, H., Magdalenić, J., & Gopalswamy, N. 2001, A&A, 377, 321
Vršnak, B., & Cliver, E. W. 2008, SoPh, 253, 215
Vršnak, B., Magdalenic, J., Aurass, H., & Mann, G. 2002, A&A, 396, 673
Wang, W., Zhu, C., Qiu, J., et al. 2019, ApJ, 871, 25
Wuelser, J.-P., Lemen, J. R., Tarbell, T. D., et al. 2004, Proc. SPIE, 5171, 111
Zhang, P., Zucca, P., Sridhar, S. S., et al. 2020, A&A, 639, A115
Zimovets, I., Vilmer, N., Chian, A. C. L., Sharykin, I., & Struminsky, A. 2012, A&A, 547, A6
Zucca, P., Carley, E. P., Bloomfield, D. S., & Gallagher, P. T. 2014, A&A, 564, A47
Zucca, P., Morosan, D. E., Rouillard, A. P., et al. 2018, A&A, 615, A89